

1
2
3
4
5
6
7
8
9
10
11
12
13
14
15
16
17
18
19
20
21
22
23
24
25
26
27
28
29
30
31
32
33
34
35
36
37
38
39
40
41
42
43
44
45
46
47
48
49
50
51
52
53
54
55
56
57
58
59
60
61
62
63
64
65

Mechanistic insights into sulfate and phosphate-mediated hexavalent chromium removal by tea polyphenols wrapped nano-zero-valent iron

Changsheng Du^{1,2}, Nan Xu^{1,2,*}, Zihan Yao^{1,2}, Xu Bai³, Yuxi Gao³, Lei Peng^{1,2}, Baohua Gu⁴,

Jiating Zhao^{3,*}

¹ School of Environmental Science and Engineering, Suzhou University of Science and Technology, Suzhou 215009, China

² Jiangsu Key Laboratory of Environmental Functional Materials, Suzhou University of Science and Technology, Suzhou 215009, China

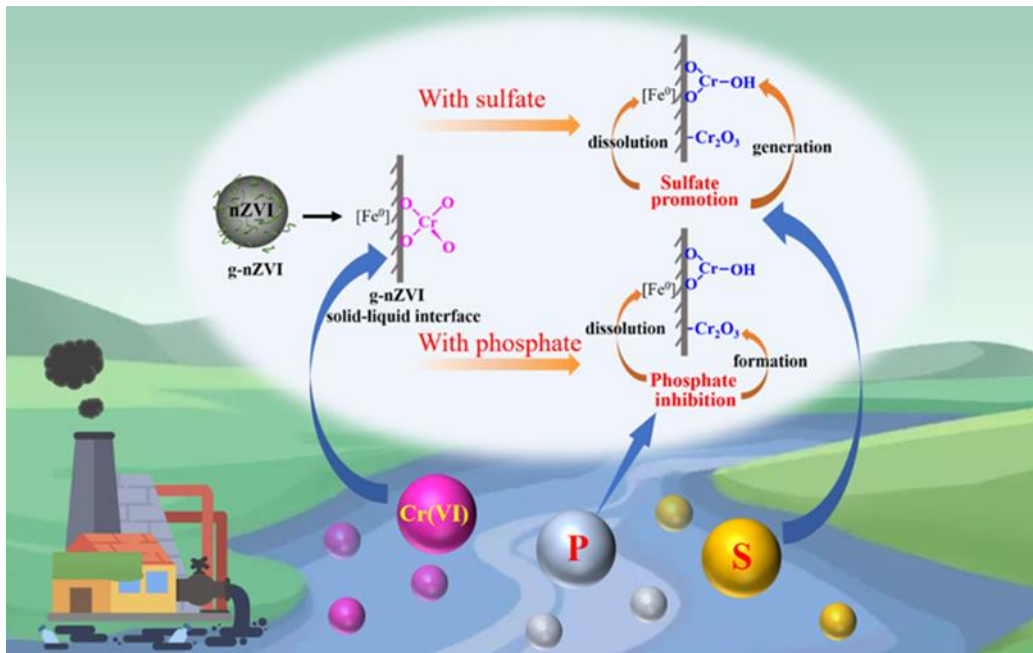
³ Key Laboratory for Biomedical Effects of Nanomaterials and Nanosafety, Institute of High Energy Physics, Chinese Academy of Sciences, Beijing 100049, P. R. China

⁴ Environmental Sciences Division, Oak Ridge National Laboratory, Oak Ridge, Tennessee 37831, United States

*Corresponding Authors:

Dr. Nan Xu, E-mail: nanxu@mail.usts.edu.cn

Dr. Jiating Zhao, E-mail: Zhaojt@ihep.ac.cn



Graphical Abstract

1 **ABSTRACT**

2 Nano zero-valent iron via green synthesis (g-nZVI) has great potential in removing toxic hexavalent
3 Cr(VI) from industrial wastewater, but sulfate and phosphate in wastewater can influence Cr(VI)
4 removal by g-nZVI. In this study, Cr(VI) removal kinetics by different g-nZVI materials were
5 investigated in the presence of sulfate and/or phosphate, and the corresponding mechanisms were
6 revealed using multiple characterizations, including X-ray absorption near-edge spectra (XANES)
7 and X-ray photoelectron spectroscopy (XPS). The results showed that Cr(OH)₃ was the dominant
8 species initially formed on the surface of g-nZVI particles before transforming to Cr₂O₃ during the
9 reaction of g-nZVI with Cr(VI). Sulfate in wastewater increased the reduction from Cr(VI) to
10 Cr(OH)₃ by g-nZVI, because sulfate promoted the release of Fe(II) and tea polyphenols (from tea
11 extracts) from the g-nZVI surface due to the corrosion of Fe⁰ core, evidenced by an increase in
12 pseudo-second-order rate constant (k_2) and subtle change in Cr(VI) removal capacity (q_e). However,
13 phosphate decreased g-nZVI corrosion and inhibited q_e because of the inner-sphere complexation of
14 phosphate onto g-nZVI, resulting in decreased release of Fe(II). When sulfate and phosphate
15 coexisted in the contaminated water, the inhibition effect of phosphate in Cr(VI) removal by g-nZVI
16 was stronger than the enhancement effect of sulfate. Accordingly, q_e value of g-nZVI declined from
17 93.4 mg g⁻¹ to 77.5 mg g⁻¹, while k_2 remained constant as the molar ratio of phosphate/sulfate
18 increased from 0.1 to 10 in water. This study provides new insights into applying g-nZVI in efficient
19 Cr(VI) removal from contaminated waters with high levels of sulphates and phosphates.

20 **Keywords:** Chromium, Sulfate, Phosphate, Green synthesized nano-zero-valent iron (g-nZVI)

1. Introduction

With rapid industrial development, wastewater heavily laden with chromium (Cr) from various industrial sources (such as chemical, tanning, metallurgy, and electroplating) has severely contaminated surface water and groundwater (Bahemmat et al., 2016; Dong et al., 2016; Su et al., 2016). In general, Cr exists mainly in two valence states in nature: trivalent chromium (Cr(III)) and hexavalent chromium (Cr(VI)) (Xiao et al., 2020). Cr(VI) is substantially more hazardous than Cr(III) because of its mutagenic, carcinogenic, teratogenic, and mobile properties (Bratovic et al., 2021; Lv et al., 2019; Yi et al., 2020). Cr(VI) concentration in industrial wastewater usually raised up to 270 mg L⁻¹ (Bratovic et al., 2021), much higher than 0.5 mg L⁻¹ of Integrated Wastewater Discharge Standard in China (GB 8978-1996). Hence, Cr(VI) removal from industrial wastewater (i.e., electroplating and tannery wastewater) is of great importance and highly desired.

Currently, nano zero-valent iron (nZVI) is an effective sorbent or reductant to remove heavy metals, organic matter, and other pollutants in water (Ahmad et al., 2021; Liao et al., 2021; Liu et al., 2022a). Nonetheless, the application of nZVI is limited due to its easy oxidation and agglomeration (Liao et al., 2021). To improve its reactivity, researchers developed many methods to modify nZVI, for example, metal hybridization, entrapment, and support were adopted to stabilize nZVI avoiding nanoparticle agglomeration (Sun et al., 2017, 2019, 2022; Vilardi et al., 2019). These common modifications were conducted via chemical methods involving the release of toxic by-products, expensive reducing reagent borohydride, and high energy consumption (Nasiri et al., 2019). By contrast, the environmentally friendly green synthesized nZVI (g-nZVI), with low cost using plant extracts, has attracted attention for pollutant removal (Fazlzadeh et al., 2017; Muhammad et al., 2019).

Such interest is attributed to the high stability, low agglomeration, and high reactivity of g-nZVI derived from Fe⁰ cores coated with tea polyphenols (TPs) (Yang et al., 2021; Ye et al., 2021).

Cr(VI) removal via g-nZVI, however, could be influenced by the chemical compositions in wastewater. Sulfate (SO₄²⁻) is a common contaminant in many industries, such as mining, textile dyeing, and tanneries, usually together with Cr(VI) (Hallam et al., 2021; Wenzel et al., 2010). Many countries set the maximum SO₄²⁻ concentration in industrial wastewater and mine drainage up to 500 mg L⁻¹ (Silva et al., 2012). Sulfate can be adsorbed on the outer sphere of metal-oxide surfaces, and its maximum adsorption capacity on natural hematite reaches 45.9 μmol g⁻¹ at pH 3 with adsorption increases with acidity (Sadeghalvad et al., 2021). As reported previously, the low concentration of sulfate (< 0.5 mg L⁻¹) can minimize Cr(VI) removal efficiency (Wang et al., 2015), as sulfate forms surface complexes with iron oxides, generating the passivation layer on the chemically synthesized nZVI (Shang et al., 2017; Xie and Cwiertny, 2012). High sulfate concentrations (>100 mg L⁻¹) can facilitate the regeneration of Fe(II) by reacting with nZVI to accelerate the electron transfer, serving as a corrosion promoter (Tang et al., 2012; Wang et al., 2015). In addition, sulfidation via chemical synthesis can enhance the reactivity and selectivity of nZVI for contaminants (Li et al., 2017; Xu et al., 2021), because soluble sulfate as by-product could be generated during the reaction of sulfurized nZVI with Cr(VI), which further increases the Cr(VI) removal (Lv et al., 2018). Moreover, materials with varying structures and morphologies have different physicochemical characteristics (Mondal et al., 2020). The green synthesized g-nZVI covered by TPs exhibits different reactivity for Cr(VI) removal from chemically synthesized nZVI due to variations in surface characteristics (Yang et al., 2021; Ye et al., 2021). Thus, sulfate might influence the reactions between TP-wrapped g-nZVI and

Cr(VI) in water.

Industrial wastewaters, especially from electroplating and detergent manufacturing, may contain more than 10 mg L⁻¹ of phosphate (Mezenner and Bensmaili, 2009). Cr(VI) and phosphate usually coexist in wastewater from mineral processing and electroplating (Wang et al., 2013). Phosphate has strong adsorption on nZVI (Wen et al., 2014) and metal (hydro) oxides (such as FeO (Guaya et al., 2021), Fe(OH)₃ (Hilbrandt et al., 2019), ZnO (Wei et al., 2021), and zirconium (IV) (Awual et al., 2011)), due to the formation of inner-sphere complexes (Tang et al., 2012). As reported, phosphate can suppress Cr(VI) adsorption because of the competitive adsorption on ferric hydroxide (Hilbrandt et al., 2019). Moreover, phosphate can complex with many metal ions, including Fe(II)/Fe(III) (Zheng et al., 2019). However, few studies have reported the mechanism by which phosphate affects the Cr(VI) removal by g-nZVI via green synthesis.

Researchers so far have only studied one single factor on the Cr(VI) removal by nZVI adsorbents (Wang et al., 2013; Xie et al., 2012). However, the co-existing anions can influence Cr(VI) removal by nZVI-Fe₃O₄ nanocomposites (Lv et al., 2013). Thus, sulfate (S) and phosphate (P), as ubiquitous anions that commonly coexist with Cr(VI) in electroplating and tanneries wastewaters (Cai et al., 2019; Wenzel et al., 2010), may play critical roles in mediating the interaction between Cr(VI) and g-nZVI. These roles prompted the necessity to investigate the underlying mechanisms of these reactions due to the complexity and diversity of the industrial wastewaters. Currently, X-ray absorption near-edge spectra (XANES) has been employed to reveal the underlying mechanisms of Cr(VI) removal by nZVI. Cr(VI) forms an outer-sphere complex on iron oxide and is then reduced to Cr(OH)₃ or Fe_xCr_{1-x}(OH)₃ (Abdullah et al., 2017; Pinakidou et al., 2016; Sheng et al., 2016). Nevertheless, there

is little information available on the effect of sulfate and/or phosphate on the Cr(VI) removal by the green synthesized g-nZVI at the molecular level.

Our previous study investigated the synthesis of modified g-nZVI composites, their applications in Cr(VI) in-situ remediation in soils, and their transport behavior in contaminated soils during remediation (Yang et al., 2021; Ye et al., 2021). For the optimized use of g-nZVI in wastewater, the effects of sulfate and phosphate on Cr(VI) removal with g-nZVI were investigated in this study. Specifically, the dissolution kinetics, zeta potentials, and particle sizes of g-nZVI impacted by sulfate and phosphate were explored. The underlying mechanisms for the speciation transformation of Cr(VI) to Cr(III) by g-nZVI in the presence of sulfate and phosphate were uncovered using multiple characterization methods including X-ray photoelectron spectroscopy (XPS) and XANES. Our results provided new insights into the practical application of g-nZVI in Cr(VI) remediation in a complex system where both sulfate and phosphate exist in aquatic environments.

2. Materials and methods

2.1. Green synthesis of various g-nZVI materials

The activity and selectivity of nZVI can be enhanced by modification with sulfide (Xu et al., 2021). In addition, ferric sulfate as an iron source can introduce sulfate into the structure of nZVI and favors Cr(VI) removal (Yang et al., 2021). This is because sulfate might remove the Fe passive oxide film and facilitate the regeneration of Fe^{2+} by reacting with nZVI (Mayer et al., 2001). Accordingly, the various g-nZVI composites (modified by sulfide and sulfate) were synthesized via green tea (Beijing Liyuan Xianshan Tea Co., Ltd.) extracts using a modified method (Wu et al., 2021; Toli et al., 2021). The total amount of TPs in the green tea extracts in the experiments ranged from 67.6-102 mg g⁻¹,

and the main reducing substances in TPs were catechins (Ye et al., 2021; Zhang et al., 2018). The detailed characterization of TPs was reported in our previous studies (Cheng et al., 2021; Ye et al., 2021) and described in Text S2 in the supporting information (SI). First, the extracts were vacuum filtered. A solution of iron chloride ($\text{FeCl}_3 \cdot 6\text{H}_2\text{O}$) or iron sulfate ($\text{Fe}_2(\text{SO}_4)_3 \cdot x\text{H}_2\text{O}$) was added to the tea extracts (TPs) to synthesize nZVI by a bottom-up approach (Machado et al., 2014), which was defined as g-nZVI and SO_4 -g-nZVI materials, respectively. Accordingly, the Fe content in the final product was about 6.7% and 9.3%. Meanwhile, S-g-nZVI (modified by sulfide with Fe content of 7.5%) was also prepared by injecting 1.0 M $\text{Na}_2\text{S} \cdot 9\text{H}_2\text{O}$ solution (S/Fe molar ratio = 0.056) into green tea extracts during g-nZVI synthesis process (Shao et al., 2018; Xu et al., 2020). The synthesis details of various g-nZVI are provided in Text S1 in SI.

2.2. Characterization analysis

Changes in the crystal phase structure of g-nZVI before and after the reaction were determined by Advance X-ray diffractometer (XRD) using a D8 Advance X-ray diffractometer (Bruker, Germany) at 40 kV and 40 mA. Operation of characterization item can refer to the literature (Li et al., 2022; Zhang et al., 2022). The functional groups and the surface morphologies of the samples were identified by Fourier transform infrared spectroscopy (FTIR, Nicolet iS10, Thermo Fisher Scientific, USA) and scanning electron microscopy (SEM, FEI Quanta 400 FEG, USA) (Pan et al., 2022b; Zeng et al., 2022). XPS (ESCALAB 250 XI, Thermo Fisher Scientific, USA) was used to determine the chemical bonding state of the samples (Liu et al., 2022b; Pan et al., 2022a). To better understand the reaction mechanisms, the hydrodynamic radius (HR) of the reaction particles was examined by the

Zeta-sizer Nano ZS90 (Malvern Instruments Ltd., UK), and the zeta potential (ZP) was determined with light scattering (DLS) at room temperature. The experimental methods were similar to previous research (Xu et al., 2019).

The XANES analyses of Cr K-edge and Fe K-edge were carried out on the beamline 1W1B (2.5 GeV, 250 mA) at the Beijing synchrotron radiation facility (BSRF). Homogenized powders from the freeze-dried bottom slurry (after reaction) were pressed into a 1 mm-thick tablet. The linear combination fitting (LCF) of the XNAES spectra was applied to quantify the major Fe and Cr species in g-nZVI (post-reaction) using the reference materials: Cr(VI) ($\text{Na}_2\text{Cr}_2\text{O}_4$), Cr(OH)₃, Cr(III) oxide (Cr_2O_3), Fe (Fe^0), ferrous oxide (FeO), and hematite (Fe_2O_3). The background and baseline spectra were corrected and normalized using the ATHENA algorithms in the Demeter computer package.

2.3. Kinetics experiments

Kinetic experiments of Cr(VI) removal by various g-nZVI materials (section 2.1) were conducted in 1.0 mM NaCl electrolyte solution on a radial vibrator. Here, 1.0 mM sulfate was injected into the suspension of 0.5 g L⁻¹ g-nZVI with and without 50 mg L⁻¹ Cr(VI), and the solution pH was adjusted to pH 2.0±0.05 by HCl solution (1.0 M) to simulate tanning and industrial electroplating wastewater, which was similar to previous studies (Wenzel et al., 2020; Tao et al., 2022; Zhu et al., 2018). Meanwhile, phosphate stock solution was injected into g-nZVI and Cr(VI) suspension with different molar ratios versus sulfate (0.5, 1, and 10). Samples were obtained at certain time intervals within 300 min before filtering through a 0.45 mm membrane. Finally, the contents of different forms of Cr and Fe in the supernatant were analyzed, and the Cr(VI) removal efficiency was calculated by equations included in Text S3 in SI (Ye et al., 2021). The dissolution kinetics affected by TPs on g-

nZVI with the presence of sulfate and phosphate were conducted, and the relevant methods were included in Text S4 in SI. Finally, Cr(VI) removal by g-nZVI under various conditions were simulated by the pseudo-second-order kinetic model (Wang et al., 2019):

$$\frac{t}{q_t} = \frac{1}{k_2 q_e^2} + \frac{t}{q_e} \quad (1)$$

where q_e and q_t represent the removal capacity at equilibrium and at different times (mg g^{-1}), respectively; k_2 is a rate constant for the pseudo-second-order ($\text{g mg}^{-1} \text{min}^{-1}$).

2.4. Concentration analysis

The concentrations of dissolved Fe(II) and aqueous Cr(VI) in the filtrate were also measured by diphenylcarbazide colorimetry method (USEPA Method 7196A) at the wavelength of 540 nm (Ryan and Hynes, 2008) and phenanthroline spectrophotometric method at 510 nm (Shao et al., 2018), respectively, using a UV-vis spectrophotometer (Shimadzu UV-1800, Japan). The total Fe and total Cr concentrations in the supernatant solution were determined by flame atomic absorption spectrometry after digestion using 5 mL HNO_3 and 10 mL HCl (1:1) with a total volume of 100 mL at 220 °C (Singh et al., 2011). All the experiments were in duplicates, and the data were the arithmetic mean of determinations with relative errors <5%.

3. Results and discussion

3.1. Cr(VI) removal by various g-nZVI materials

The kinetic experiment revealed the Cr(VI) removal rate by various g-nZVI composites at different times. Figs. 1a–1c show the variations in Cr speciation (including Cr(VI), Cr(III), and particulate Cr) and the dissolved Fe(III) during Cr(VI) removal by three g-nZVIs (i.e., g-nZVI, SO_4 -g-nZVI, and S-

g-nZVI). In general, the Cr(VI) concentration sharply decreased during initial 50 min, with a high proportion removed by different g-nZVI materials (Figs. 1a–1c). Specifically, the control of g-nZVI completely removed Cr(VI) at 180 min equilibrium time, where 51.9% Cr(VI) was converted to soluble Cr(III) and the remaining Cr species existed as particulate Cr (Fig. 1a), which includes the adsorbed Cr(VI) and the precipitated/complexed Cr(III) (Xu et al., 2022). Compared to the Cr(VI) removal capacity (35.2 mg g^{-1}) of nZVI prepared by chemical synthesis (Zhu et al., 2018), g-nZVI in this study had a significantly higher capacity (100 mg g^{-1}), likely resulting from TPs coverage on the surface which prevented g-nZVI from oxidation and thus increased Cr(VI) removal. In addition, the similar experiment was carried out to explore the possibility of the released TPs for Cr(VI) reduction. The reactions between Cr(VI) and the released TPs in the filtrate of g-nZVI suspension were conducted at pH 6.8, given that only TPs could be released from g-nZVI into solution and little Fe(II) generated. The results showed that the amount of Cr(VI) reduction by TPs released by g-nZVI was negligible (0.02 mg L^{-1} via UV-vis spectra analysis). Therefore, the Cr(VI) could not be reduced directly by TPs.

As shown in Fig. 1b, SO_4 -g-nZVI (prepared from iron sulfate) removed Cr(VI) entirely at 120 min, while Cr(VI) removal rate of g-nZVI (prepared from iron chloride) reached the maximum at 180 min (Fig. 1a), which implies a faster Cr(VI) removal rate by SO_4 -g-nZVI than g-nZVI (SI Fig. S3). The pseudo-second-order kinetic model was applied to simulate the Cr(VI) removal at different times (Fan et al., 2020; Singh et al., 2021). The fitting results show that the q_e of Cr(VI) by SO_4 -g-nZVI was 103.1 mg g^{-1} , which was similar to that of g-nZVI (Table S1 in the SI). Correspondingly, the k_2 value of SO_4 -g-nZVI was $16.1 \times 10^{-4} \text{ g mg}^{-1} \text{ min}^{-1}$, which was significantly higher than $8.5 \times 10^{-4} \text{ g}$

$\text{mg}^{-1} \text{min}^{-1}$ of g-nZVI (Table S1). This result could be because sulfate helped to remove the passive oxide film of iron, promoting Fe^0 corrosion (Lv, et al., 2018). This observation was consistent with the higher dissolved Fe(III) concentrations (Fig. 1b vs. 1a, and Fig. S3b). Accordingly, sulfate can facilitate the regeneration of Fe(II) through the reaction with Fe^0 to accelerate Cr(VI) removal (Tang et al., 2012; Lv et al., 2018).

The S-g-nZVI could remove Cr(VI) completely from water within 200 min, which was similar to SO_4 -g-nZVI and g-nZVI (Fig. 1c vs. 1a and 1b). Nevertheless, the Cr(VI) removal rate of S-g-nZVI in 50 min was faster than that of SO_4 -g-nZVI and even g-nZVI (Fig. S3a in the SI). This result agrees with the kinetic model results that the k_2 value of S-g-nZVI was $41.8 \times 10^{-4} \text{ g mg}^{-1} \text{ min}^{-1}$, which was higher than that of g-nZVI and SO_4 -g-nZVI, although the S-g-nZVI has a similar q_e (101.0 mg g^{-1}) of Cr(VI) removal as g-nZVI and SO_4 -g-nZVI (Table S1). This was likely because the efficiency (54.8%) in forming Cr particulates by S-g-nZVI was greater than 46.1% for SO_4 -g-nZVI at 50 min of reaction time (Fig. 1c vs. 1b). Meanwhile, a lower dissolution rate (45.2%) of Cr(III) by S-g-nZVI than 53.9% by SO_4 -g-nZVI was observed. In other words, the lower dissolution of Cr(III) led to more Cr(III) precipitation and formation of Cr particulates (including Cr(III) precipitation and Cr(VI) adsorption). As previously reported, sulfidation could enhance the reaction activity and surface adsorption sites of nZVI (Lv et al., 2019). In addition, the q_e of S-g-nZVI for Cr(VI) was greatly higher than that of chemically synthesized S-nZVI (59.9 mg g^{-1}) (Lv et al., 2019). Such a scenario is possible due to the wrapping of S-g-nZVI by TPs layers, thereby reducing the agglomeration of Fe^0 nanoparticles and improving their stability and reactivity (Ye et al., 2021).

3.2. Effects of sulfate on Cr(VI) removal by g-nZVI

To clarify the role of sulfate on Cr(VI) removal, we investigated Cr species transformation by g-nZVI in the presence of sulfate. The q_e of g-nZVI obtained from the pseudo-second-order kinetic model remained similar in the presence of 1 mM sulfate as shown in Table S1, which was consistent with the slight change in the Cr(III) dissolution efficiency from 51.9% to 57.3% and in the generation efficiency of particulate Cr (including Cr(III) precipitation and Cr(VI) adsorption) from 48.2% to 42.7% at 120 min of the reaction time (Fig. 1d vs. Fig. 1a). Nevertheless, the Cr(VI) removal rate k_2 of g-nZVI significantly increased from 8.5×10^{-4} to $18.7 \times 10^{-4} \text{ g mg}^{-1} \text{ min}^{-1}$ when sulfate was present, which was consistent with the promoted dissolution of Fe(III) by g-nZVI reaction with Cr(VI) from 60.4% to 76.1% (Fig. 1d vs. Fig. 1a). This implies that sulfate could induce fast corrosion of g-nZVI for Cr(VI) removal.

3.3. Effects of sulfate and phosphate on Cr(VI) removal by g-nZVI

Cr(VI) removal kinetics by g-nZVI were further investigated under complex conditions and various P/S molar ratios in water. The Cr(VI) removal efficiency by g-nZVI initially reduced from 100% to 88.0% in the presence of 0.5 mM phosphate (Fig. 2a), which was attributed to the inhibition in Cr(VI) reduction to soluble Cr(III) by Fe(II) released from g-nZVI (Figs. 2c and 2d), although phosphate can decrease Cr(VI) removal due to competitive adsorption (Hilbrandt et al., 2019). Accordingly, the q_e decreased from 104.6 to 92.3 mg g^{-1} with the presence of phosphate alone in aqueous solution, while the change of k_2 is unobvious (Table S1). When 0.5 mM phosphate and 1 mM sulfate coexisted (P/S molar ratio = 0.5), the Cr(VI) removal efficiency of g-nZVI to Cr(VI) was less than that of control (Figs. 2a and 2b) because the dissolved Fe(II) in the copresence of sulfate and phosphate was lower than the control by g-nZVI alone (Fig. 2c). Moreover, with different P/S molar ratios, the dissolved

Fe(II) concentration from g-nZVI rapidly increased in the initial 20 min and then slowly reached a plateau (Fig. 2c), which agreed with the Cr(VI) removal kinetics of g-nZVI (Fig. 2a). Interestingly, the generation capacity of soluble Cr(III) by g-nZVI reduced from 47.2 mg g⁻¹ to 40.4 mg g⁻¹, whereas the particulate Cr lowered from 44.9 mg g⁻¹ to 32.0 mg g⁻¹ with increasing the P/S molar ratio from 0.5 to 10 (Fig. 2b). The corresponding q_e was observed decreased from 93.4 mg g⁻¹ to 77.5 mg g⁻¹ associated with a consistent k_2 value (Table S1). This phenomenon indicated that phosphate significantly hindered the Cr(VI) removal capacity q_e of g-nZVI, even with the coexistence of sulfate. This result was also consistent with the phenomenon that the inhibition of Fe(II) release from g-nZVI by phosphate was more predominant than the enhancement by sulfate (Fig. 2d). The phosphate inner-sphere complexes on the surface of iron (oxy) hydroxides could hinder the corrosion of Fe⁰ cores to lower Cr(VI) removal (Tanboonchuy et al., 2012). Furthermore, phosphate had a similar structure and size to CrO₄²⁻/HCrO₄⁻ and could thus compete with Cr(VI) adsorption on g-nZVI. However, sulfate is primarily adsorbed as an outer-sphere complex with a small inner sphere, which can accelerate electron generation as a corrosion promoter to improve Cr(VI) removal (Jing et al., 2018; Xie and Cwiertny, 2012). Accordingly, the inner sphere complexes of phosphate showed a more significant effect on the solid–water interface reactions between g-nZVI and Cr(VI) than that of sulfate outer-sphere complexes. In addition, the kinetics of TPs release from g-nZVI surface with the presence of sulfate or phosphate, compared with that of g-nZVI alone, showed that phosphate hindered the TPs released from g-nZVI, whereas sulfate promoted TP release (Fig. S4). A detailed explanation on the role of sulfate and phosphate in the release of TPs from g-nZVI was concluded in Text S4 in SI. Overall, the pseudo-second-order kinetic model showed that sulfate mainly promoted k_2 while

phosphate inhibited q_e for Cr(VI) removal by g-nZVI.

3.4. Mechanisms

3.4.1. Zeta potential and hydrodynamic radius analysis

To better understand the Cr(VI) removal mechanism by g-nZVI with the coexistence of sulfate and phosphate, the surface properties of g-nZVI with Cr(VI) were investigated. Surface ZPs of g-nZVI were negatively charged (-35.9 mV) in 1 mM NaCl solution (Fig. S5), which was similar to a previous report (Kumar et al., 2015). The particle surface of g-nZVI became positively charged after reaction with Cr(VI) (Fig. S5a), due to the reduced Cr(III) adsorption. Accordingly, the repulsion forces between g-nZVIs decreased based on Derjaguin–Landau–Vervey–Overbeek theory (Cheng et al., 2018). Thus, the g-nZVI nanoparticles easily aggregated and became significantly increased in size (Fig. S5b).

When phosphate or sulfate was present in the solution, the positive surface charges of g-nZVI particles with Cr were further reduced by phosphate or sulfate adsorption, leading to the increase of particle size from 458.7 nm to 615 nm (phosphate) and 531.2 nm (sulfate) as previously discussed (Fig. S5b). In the copresence of phosphate and sulfate, the absolute values of particle surface potential gradually decreased at high P/S molar ratios (Fig. S5a), thereby lessening the repulsion forces between the nanoparticles due to the competitive adsorption of both sulfate and phosphate onto g-nZVI. This phenomenon confirmed that the large particles formed from approximately 712.4 to 825.0 nm with increasing P/S molar ratios (0.5–10; Fig. S5b).

3.4.2. SEM analysis

SEM micrographs of the synthesized g-nZVI showed that the sizes and shapes of nanoparticles

were similar, indicating that the particles were distributed uniformly (Fig. S6a). The surface of pristine g-nZVI was composed of carbon (C), oxygen (O), and iron (Fe) in element mapping, revealing that the g-nZVI was composed of black Fe⁰ core covered with a layer of TPs (Ye et al., 2021). After that, the nanoparticles accumulated loosely with relatively large accumulated pores due to the reactions with Cr(VI) (Fig. S6b). In the presence of sulfate and phosphate, an intense Cr peak and a weak Fe peak were observed in the EDS spectra of g-nZVI sample (Fig. S6d vs. Fig. S6c), indicating that Fe⁰ cores corroded from g-nZVI after reacting with Cr. In addition, SEM/EDS analyses of S and P (Figs. S5b and S5d) indicated that sulfate and phosphate might be adsorbed on the surface of the material. Moreover, the proportion of phosphate (1.8%) was greater than sulfate (0.5%), likely because the phosphate adsorption was stronger than that of sulfate (Jing et al., 2018).

3.4.3. XRD and FTIR analyses

The synthesized g-nZVI exhibited amorphous morphology as shown in Fig. S7a, which was in agreement with the low resolution of the XRD peak at $2\theta = 25^\circ$ indicating the Fe⁰ core wrapped by excessive TP coverage (Fig. S7). Thus, FTIR analysis was employed to investigate the functional groups on g-nZVI with Cr(VI) when sulfate and/or phosphate were present. As shown in Fig. 3, the g-nZVI surface had abundant functional groups. The peaks at 1626 and 1713 cm⁻¹ were identified as C=C or C=O (Choudhary et al., 2017; Lin et al., 2020; Zhang et al., 2020), whereas those at 1050 and 1092 cm⁻¹ as C-O (Dong et al., 2011), which corresponded to peculiar substances of TPs or catechol from green tea. These findings confirmed that g-nZVI was successfully synthesized via TP extraction from green tea and acted as a reducing, capping agent.

By increasing the Cr(VI) concentration from 50 mg L⁻¹ to 200 mg L⁻¹ (Fig. 3a), the IR

characteristic peaks of g-nZVI at 1050 and 1092 cm^{-1} associated with the C–O group disappeared and gradually broadened, respectively. This phenomenon was possible due to the partial corrosion of Fe^0 cores (Fig. 2b) leading to the TP release from g-nZVI during the reaction with Cr(VI) (Yang et al., 2021; Ye et al., 2021).

When a low concentration of sulfate was added, the peaks of C–O group at 1050 and 1092 cm^{-1} were still found for g-nZVI (Fig. 3b). As the sulfate concentration increased from 50 to 200 mM, a new peak was observed at 622 cm^{-1} associated with Fe–O stretching vibration. Particularly, a new peak at 1112 cm^{-1} representing the SO_4^{2-} bending vibration appeared, instead of peaks at 1050 and 1092 cm^{-1} . These changes may be attributed to sulfate adsorption by g-nZVI, causing the “redshift” of the C–O peak to 1112 cm^{-1} (Jing et al., 2018; Xie and Cwiertny, 2012; Yao et al., 2020). In addition, more exposure of iron oxides ensued due to the unwrapped TP coverage around green synthesized nZVI, induced by sulfate (Yang et al., 2021; Ye et al., 2021). Therefore, in the copresence of Cr(VI) and sulfate, new peaks at 1112 and 622 cm^{-1} appeared whereas that the peak at 1050 cm^{-1} disappeared (Fig. 3d). This result is consistent with a previous kinetic experiment where sulfate was found to promote g-nZVI corrosion and improved Cr(VI) removal (Figs. 2b and 2d).

In the presence of phosphate alone, the peaks of g-nZVI at 1050 and 1092 cm^{-1} , associated with the C–O group, merged with a strong and broad peak at 1080 cm^{-1} as the phosphate concentration increased from 50 to 200 mg L^{-1} (Fig. 3c). This change indicated that phosphate chemically adsorbed (C–O bond) onto g-nZVI via inner-sphere coordination. As shown in Fig. 3d, the peaks at 1050 and 1092 cm^{-1} (C–O) of g-nZVI reaction with Cr(VI) broadened in the presence of phosphate. This change ensued because phosphate and Cr(VI) were simultaneously adsorbed on g-nZVI, resulting in

less Cr(VI) adsorption due to competitive adsorption. Also, the broadened peak of C–O at 1092 cm^{-1} might be attributed to the re-adsorption of dissolved organic matter onto g-nZVI since TPs coverage could release from the g-nZVI surface as shown in Fig. S4.

3.4.4. XANES and XPS analyses

XANES and XPS analyses were performed on g-nZVI with or without Cr(VI) when sulfate or phosphate was also present. The XAFS spectra of g-nZVI after reaction with 50 mg L^{-1} Cr(VI) showed the coordination characteristic peaks at approximately 1.50 and 1.54 \AA arising from Fe-O and Cr-O (Figs. 4a and 4b), respectively. These peaks indicate that the surface of g-nZVI has been oxidized to iron oxide by Cr(VI). Furthermore, the sample's Cr K-edge of XANES was markedly different from the Cr_2O_3 and $\text{Na}_2\text{Cr}_2\text{O}_7$ standards, and the spectra showed a wide peak at 6075.6 eV and a strong peak at 6007.7 eV where both are associated with Cr(III) speciation as $\text{Cr}(\text{OH})_3$ formation (Fig. 4c). LCF analysis of the XANES spectra further revealed that $\text{Cr}(\text{OH})_3$ was the dominant species on g-nZVI (Fig. S8), suggesting that Cr(VI) at low concentrations has been substantially reduced to $\text{Cr}(\text{OH})_3$ by g-nZVI.

When solution Cr(VI) was increased to 200 mg L^{-1} , the corresponding XPS full-spectra of g-nZVI associated with Fe 2p, C 1s, and O 1s peaks were depicted in Fig. S9a in SI. Notably, the Cr 2p spectrum confirmed 43.7% $\text{Cr}(\text{OH})_3$ (577.8 eV), 37.8% Cr_2O_3 (576.8 eV), and 18.5% Cr(VI) on g-nZVI (Fig. 5b). This result indicated that $\text{Cr}(\text{OH})_3$ and Cr_2O_3 simultaneously occurred on nanomaterials (Yang et al., 2021). Therefore, these findings suggest that $\text{Cr}(\text{OH})_3$ formed first before the formation of Cr_2O_3 as Cr(VI) was transformed to Cr(III) (Fig. S8a and Fig. 5b).

In the presence of sulfate, Cr(VI) at low concentrations was completely reduced to $\text{Cr}(\text{OH})_3$ by g-

nZVI based on the Cr K-edge XANES spectra analysis (Fig. 4c). When the sulfate concentration was raised to 200 mg L⁻¹, a new peak of S 2p, ascribed to Fe₂(SO₄)₃, was detected at 169.2 eV in the full XPS spectrum (Figs. S9b and S10g) (Yao et al., 2020). The presence of sulfate significantly increased the proportion of Fe(II) (FeO, 710.9 eV; Fe(II) satellite, 714.5 eV) from 75.5% to 81.7% (Fig. 5a vs. 5c). In response, the Fe₂O₃ decreased from 24.5% to 18.3%. Meanwhile, the Fe-O peak at 531.8 eV decreased from 24.0% to 21.2% (Fig. S10d vs. Fig. S10b). Accordingly, the Cr(VI) peak at 579.2 eV shrank from 18.5% to 16.7% (Fig. 5d vs. Fig. 5b). Note that Cr(OH)₃ (577.8 eV) significantly increased from 43.7% to 65.6%, whereas Cr₂O₃ (576.8 eV) decreased from 37.8% to 17.7% (Fig. 5d vs. 5b), possibly because sulfate (as a corrosion promoter) could facilitate Fe(II) regeneration when reacting with g-nZVI as shown in Fig. 5g. This scenario favors the rapid reduction from Cr(VI) to Cr(OH)₃ (Fig. 5d). In addition, the proportion of the C=O peak decreased from 9.9% to 4.5% (Fig. S10c vs. Fig. S10a), because of the promoted TP release from g-nZVI surface by sulfate (Fig. S4).

Similarly, Cr K-edge XANES spectra analysis showed that Cr(VI) at low concentrations was predominantly reduced to Cr(OH)₃ by g-nZVI regardless of the presence of phosphate (Fig. 4c). When reacting with more concentrated Cr(VI), g-nZVI showed a new peak P 2p at 707 eV, identified as FePO₄ due to the presence of phosphate (Fig. S10h) (Liu et al., 2013). Moreover, the proportion of the Fe(II) (FeO and Fe(II) satellite) peak decreased from 75.5% to 66.7% (Fig. 5a vs. Fig. 5e). Notably, the Fe-O peak of g-nZVI with Cr(VI) at 531.8 eV was 28.0% in the presence of phosphate (vs. 24.0% in the absence of phosphate) (Fig. S10f vs. Fig. S10b). Accordingly, the Cr(VI) peak increased from 18.5% to 28.2% (Fig. 5b vs. Fig. 5f), and the Cr(III) peak (including Cr(OH)₃ and Cr₂O₃) decreased from 81.5% to 71.8%. Overall, the Cr(OH)₃ formation induced by g-nZVI increased from 43.7% to

48.5%, whereas Cr_2O_3 generation lowered from 37.8% to 23.3% after phosphate was added (Fig. 5f vs. Fig. 5b). This change was most likely ascribed to the inhibition in Cr_2O_3 formation by the inner sphere complexes of phosphate with iron (oxy) hydroxides on the surface of g-nZVI (Fig. 5g), resulting in the hindered corrosion of g-nZVI to release Fe(II). In addition, the proportion of the C=O peak increased from 9.9% to 13.6% (Fig. S10a vs. Fig. S10e), because phosphate inhibited the dissolution of organic matter wrapped around the g-nZVI nanoparticles (Fig. S7).

Wastewater from traditional mineral processing, electroplating, and tanneries not only contains a large amount of Cr(VI), but also plenty of sulfate and phosphate. Thus, both sulfate and phosphate might affect the removal efficiency of Cr(VI) by green synthesized g-nZVI. The low concentration ($<50 \text{ mg L}^{-1}$) of Cr(VI) in solution could be mostly reduced to $\text{Cr}(\text{OH})_3$ by g-nZVI. Nevertheless, the high concentration ($>200 \text{ mg L}^{-1}$) of Cr(VI) is reduced to $\text{Cr}(\text{OH})_3$ and Cr_2O_3 by g-nZVI. Thus, we hypothesize that Cr(VI) is first reduced to $\text{Cr}(\text{OH})_3$ and then partially converted to Cr_2O_3 by g-nZVI. As shown in Fig. 5g, it is pertinent to mention that sulfate could promote the conversion rate of Cr(VI) to $\text{Cr}(\text{OH})_3$, as a result of the increased Cr(VI) removal rate, since sulfate as a corrosion promoter of g-nZVI can only increase the Fe(II) dissolution rate due to the out-sphere adsorption of sulfate. When phosphate and sulfate coexist, they impede the Cr(VI) removal by g-nZVI due to the greater inhibition effect through inner-sphere complexation of phosphate. In particular, phosphate could lower the g-nZVI corrosion to produce Fe(II) and further inhibit the conversion from $\text{Cr}(\text{OH})_3$ to Cr_2O_3 , thereby hindering the Cr(VI) removal capacity by g-nZVI.

4. Conclusions

In this study, we reveal the underlying mechanisms and pathways of Cr(VI) removal by TPs encapsulated g-nZVI in contaminated water with enrichment of sulfate and phosphate. Generally, sulfate promoted Cr(VI) removal by g-nZVI, whereas phosphate showed a powerful inhibitory effect. This difference was attributed to the presence of sulfate, a corrosion promoter, which could accelerate TPs dissolution and Fe(II) generation from g-nZVI to facilitate Cr(VI) reduction to Cr(OH)₃. However, phosphate in water could adsorb and complex on the surface of g-nZVI, thereby inhibiting Fe(II) release from g-nZVI and subsequently hindering Cr(VI) reduction to Cr₂O₃. Particularly, the inhibition effect of phosphate on Cr(VI) removal was greater than the enhancement of sulfate due to the stronger inner-sphere complex of phosphate than outer-sphere adsorption of sulfate on g-nZVI with varying P/S ratios. Consequently, this work provide theoretical support for the field application of green synthesized g-nZVI in removing Cr(VI) from wastewater by controlling sulfate and phosphate concentrations.

Supporting information

Supporting information mainly includes the synthesis of various g-nZVI materials; final pH change during Cr(VI) removal; model parameters of Cr(VI) removal kinetics; XRD patterns and linear combination fitting of the XANES spectra and XPS spectra of g-nZVI under various conditions.

Acknowledgments

The authors would like to thank the financial support by National Natural Science Foundation of China (21777110). The authors also thank the Beijing Synchrotron Radiation Facility (Institute of High Energy Physics, Chinese Academy of Sciences) for granting access to their beamline. Oak Ridge National Laboratory (ORNL) is managed by UT-Battelle, LLC under Contract No. DE-AC05-

References

- Abdullah, A. M., Masao, M., Mitsuaki, M., Chiharu, T., 2017. Sorption mechanisms of chromate with coprecipitated ferrihydrite in aqueous solution. *J. Hazard. Mater.* 334, 142–149.
- Ahmad, S., Liu, X., Tang, J., Zhang, S., 2021. Biochar-supported nanosized zero-valent iron (nZVI/BC) composites for removal of nitro and chlorinated contaminants. *Chem. Eng. J.* 133187.
- Awual, M.R., Jyo, A., Ihara, T., Seko, N., Tamada, M., Lim, K.T., 2011. Enhanced trace phosphate removal from water by zirconium(IV) loaded fibrous adsorbent. *Water Res.* 45 (15), 4592–4600.
- Bahemmat, M., Farahbakhsh, M., Kianirad, M., 2016. Humic substances-enhanced electroremediation of heavy metals contaminated soil. *J. Hazard. Mater.* 312, 307–318.
- Bratovic, A., Buksek, H., Helix-Nielsen, C., Petrinic, I., 2021. Concentrating hexavalent chromium electroplating wastewater for recovery and reuse by forward osmosis using underground brine as draw solution. *Chem. Eng. J.* 431, 133918.
- Cai, W., Fu, F., Zhu, L., Tang, B., 2019. Simultaneous removal of chromium(VI) and phosphate from water using easily separable magnetite/pyrite nanocomposite. *J. Alloy. Compd.* 803, 118–125.
- Cheng, X., Wang, S., Xu, N., Yang, L., Jing, P., 2021. Enhanced transport and chromium remediation of nano-zero valent iron modified by tea polyphenol extracts and carboxymethyl cellulose in water–soil media. *J. Soil. Sediment.* 22, 196–207.
- Cheng, X., Xu, N., Huangfu, X., Zhou, X., Zhang, M., 2018. Synergetic effect of hydrochar on the transport of anatase titanium dioxide nanoparticles in the presence of phosphate in saturated quartz sand. *Environ. Sci. Pollut. R.* 25 (29), 28864–28874.
- Choudhary, B., Paul, D., Singh, A., Gupta, T., 2017. Removal of hexavalent chromium upon interaction with biochar under acidic conditions: mechanistic insights and application. *Environ. Sci. Pollut. Res.* 24 (20), 1–12.
- Dong, H., He, Q., Zeng, G., Tang, L., Zhang, C., Xie, Y., Zeng, Y., Zhao, F., Wu, Y., 2016. Chromate removal by surface-modified nanoscale zero-valent iron: effect of different surface coatings and water chemistry. *J. Colloid Interface Sci.* 471, 7–13.
- Dong, R., Liu, Y., Wang, X., Huang, J., 2011. Adsorption of sulfate ions from aqueous solution by surfactant-modified palygorskite. *J. Chem. Eng.* 56 (10), 3890–3896.
- Fan, H., Ren, H., Ma, X., Zhou, S., Liu, Y., 2020. High-gravity continuous preparation of chitosan-stabilized nanoscale zero-valent iron towards Cr(VI) removal. *Chem. Eng. J.* 390, 124639.
- Fazlzadeh, M., Rahmani, K., Zarei, A., Abdoallahzadeh, H., Khosravi, R., 2017. A novel green synthesis of zero valent iron nanoparticles (nZVI) using three plant extracts and their efficient application for removal of Cr(VI) from aqueous solutions. *Adv. Powder Technol.* 28 (1), 122–130.
- Guaya, D., Jimenez, R., Sarango, J., Valderrama, C., Cortina, J.L., 2021. Iron-doped natural clays: Low-cost inorganic adsorbents for phosphate recovering from simulated urban treated wastewater. *J. Water Process Eng.* 43, 102274.
- Hallam, L., Papasergio, A.E., Lessio M., Veliscek-Carolan, J., 2021. Phosphate functionalised titania

- for heavy metal removal from acidic sulfate solutions. *J. Colloid Interface Sci.* 600, 719–728.
- Hilbrandt, I., Ruhl, A. S., Zietzschmann, F., Molkenthin, M., Jekel, M., 2019. Competition in chromate adsorption onto micro-sized granular ferric hydroxide. *Chemosphere* 218, 749–757.
- Jing, L., Zhu, R., Liang, X., Ma, L., Molinari, M., 2018. Synergistic adsorption of Cd(II) with sulfate/phosphate on ferrihydrite: An in situ ATR-FTIR/2D-COS study. *Chem. Geol.* 477, 12–21.
- Kumar, R., Singh, N., Pandey, N., 2015. Potential of green synthesized zero-valent iron nanoparticles for remediation of lead-contaminated water. *Int. J. Environ. Sci. Technol.* 12 (12), 3943–3950.
- Li, J., Zhang, X., Sun, Y., Liang, L., Pan, B.C., Zhang, W., Guan, X., 2017. Advances in sulfidation of zerovalent iron for water decontamination. *Environ. Sci. Technol.* 248 (23), 173–182.
- Li, Z., Zhang, W., Tao, M., Shen, L., Li, R., Zhang, M., Jiao, Y., Hong, H., Xu, Y., Lin, H., 2022. In-situ growth of UiO-66-NH₂ in porous polymeric substrates at room temperature for fabrication of mixed matrix membranes with fast molecular separation performance. *Chem. Eng. J.* 435, 134804.
- Liao, M., Wang, X., Cao, S., Li, M., Peng, X., Zhang, L., 2021. Oxalate modification dramatically promoted Cr(VI) removal with zero-valent iron. *Environ. Sci. Technol.* 1, 8365–8373.
- Lin, Z., Weng, X., Owens, G., Chen, Z., 2020. Simultaneous removal of Pb(II) and rifampicin from wastewater by iron nanoparticles synthesized by a tea extract. *J. Clean. Prod.* 242, 118476.
- Liu, H., Chen, T., Zou, X., Xie, Q., Qing, C., Chen, D., Forst, R.L., 2013. Removal of phosphorus using nZVI derived from reducing natural goethite. *Chem. Eng. J.* 234 (12), 80–87.
- Liu, X., Zhang, S., Zhang, X., Guo, H., Lou, Z., Zhang, W., Chen, Z., 2022a. Cr(VI) immobilization in soil using lignin hydrogel supported nZVI: Immobilization mechanisms and long-term simulation. *Chemosphere* 224, 135393.
- Liu, J., Shen, L., Lin, H., Huang, Z., Hong, H., Chen, C., 2022b. Preparation of Ni@UiO-66 incorporated polyethersulfone (PES) membrane by magnetic field assisted strategy to improve permeability and photocatalytic self-cleaning ability. *J. Colloid Interface Sci.* 618, 483–495.
- Lv, D., Zhou, J., Cao, Z., Xu, J., Liu, Y., Li, Y., Yang, K., Lou, Z., Lou, L., Xu, X., 2019. Mechanism and influence factors of chromium(VI) removal by sulfide-modified nanoscale zerovalent iron. *Chemosphere* 224, 306–315.
- Lv, X., H, Y., Tang, J., Sheng, T., Jiang, G., Xu, X., 2013. Effects of co-existing ions and natural organic matter on removal of chromium (VI) from aqueous solution by nanoscale zero valent iron (nZVI)-Fe₃O₄ nanocomposites. *Chem. Eng. J.* 218, 55–64.
- Lv, Y., Li, Z., Jian, F., Li, J., Chen, K., Den, H., Shou, J., Li, Y., 2018. Synergetic effect of pyrite on Cr(VI) removal by zero valent iron in column experiments: an investigation of mechanisms. *Chem. Eng. J.* 349, 522–529.
- Machado, S., Grosso, J.P., Nouws, H.P.A., Albergaria, J.T., Delerue-Matos, C., 2014. Utilization of food industry wastes for the production of zero-valent iron nanoparticles. *Sci. Total Environ.* 496, 233–240.
- Mayer, K.U., Blowes, D.W., Frind, E.O., 2001. Reactive transport modeling of an in situ reactive barrier for the treatment of hexavalent chromium and trichloroethylene in groundwater. *Water Resour. Res.* 37, 3091-3103.

- Mezener, N.Y., Bensmaili, A., 2009. Kinetics and thermodynamic study of phosphate adsorption on iron hydroxide-eggshell waste. *Chem. Eng. J.* 147 (2-3), 87–96.
- Mondal, P., Anweshan, A., Purkait, M.K., 2020. Green synthesis and environmental application of iron-based nanomaterials and nanocomposite: a review. *Chemosphere* 259, 127509.
- Muhammad, F., Xia, M., Li, S., Yu, X., Mao, Y., Muhammad, F., Huang, X., Jiao, B., Yu, L., Li, D., 2019. The reduction of chromite ore processing residues by green tea synthesized nano zerovalent iron and its solidification/stabilization in composite geopolymer. *J. Clean. Prod.* 234, 381–391.
- Nasiri, J., Motamedi, E., Naghavi, M.R., Ghafoori, M., 2019. Removal of crystal violet from water using β -cyclodextrin functionalized biogenic zero-valent iron nanoadsorbents synthesized via aqueous root extracts of *Ferula persica*. *J. Hazard. Mater.* 367, 325–338.
- Pan, Z., Zeng, B., Yu, G., Teng, J., Zhang, H., Shen, L., Yang, L., Lin, H., 2022a. Mechanistic insights into Ca-alginate gel-associated membrane fouling affected by ethylene diamine tetraacetic acid (EDTA). *Sci. Total Environ.* 842, 156912.
- Pan, Z., Zeng, B., Lin, H., Teng, J., Zhang, H., Hong, H., Zhang, M., 2022b. Fundamental thermodynamic mechanisms of membrane fouling caused by transparent exopolymer particles (TEP) in water treatment. *Sci. Total Environ.* 820, 153252.
- Pinakidou, F., Katsikini, M., Simeonidis, K., Kaprara, E., Paloura, E.C., Mitrakas, M., 2016. On the passivation mechanism of Fe_3O_4 nanoparticles during Cr(VI) removal from water: A XAFS study. *Appl. Surf. Sci.* 360, 1080–1086.
- Ryan, P., Hynes, M.J., 2008. The kinetics and mechanisms of the reactions of iron(III) with quercetin and morin. *J. Inorg. Biochem.* 102 (1), 127–136.
- Sadeghalvad, B., Khorshidi, N., Azadmehr, A., Sillanp, M. Sorption, mechanism, and behavior of sulfate on various adsorbents: a critical review. *Chemosphere* 2021, 263, 128064.
- Shang, J., Zong, M., Yu, Y., Kong, X., Du, Q., Liao, Q., 2017. Removal of chromium (VI) from water using nanoscale zerovalent iron particles supported on herb-residue biochar. *J. Environ. Manag.* 197, 331–337.
- Shao, Q., Xu, C., Wang, Y., Huang, S., Tratnyek, P.G., 2018. Dynamic interactions between sulfidated zerovalent iron and dissolved oxygen: mechanistic insights for enhanced chromate removal. *Water Res.* 135, 322.
- Sheng, G., Hu, J., Li, H., Li, J., Huang, Y., 2016. Enhanced sequestration of Cr(VI) by nanoscale zero-valent iron supported on layered double hydroxide by batch and XAFS study. *Chemosphere* 148, 227–232.
- Silva, A.M. Lima, R.M.F. Leão, V.A., 2012. Mine water treatment with limestone for sulfate removal. *J. Hazard. Mater.* 221–222, 45–55.
- Singh, P., Pal, P., Mondal, P., Saravanan, G., Bhowmick, S., 2021. Kinetics and mechanism of arsenic removal using sulfide-modified nanoscale zerovalent iron. *Chem. Eng. J.* 412(6493), 128667.
- Singh, R., Misra, V., Singh, R.P., 2011. Synthesis, characterization and role of zero-valent iron nanoparticle in removal of hexavalent chromium from chromium-spiked soil. *J. Nanopart. Res.* 13 (9), 4063–4073.
- Su, H., Fang, Z., Tsang, P. E., Fang, J., Zhao, J., 2016. Stabilisation of nanoscale zero-valent iron with

- biochar for enhanced transport and in-situ remediation of hexavalent chromium in soil. *Environ. Pollut.* 214, 94–100.
- Sun, P., Wang, Z., An, S., Zhao, J., Yan, Y., Zhang, D., Wu, Z., Shen, B., Lv., H., 2022. Biochar-supported nZVI for the removal of Cr(VI) from soil and water: Advances in experimental research and engineering applications. *J. Environ. Manag.* 316, 115211.
- Sun, Y., Lei, C., Khan, E., Chen, S.S., Tsang, D.C.W., Ok, Y.S., Lin, D., Feng, Y., Li, X., 2017. Nanoscale zero-valent iron for metal/metalloid removal from model hydraulic fracturing wastewater. *Chemosphere* 176, 315–323.
- Sun, Y., Yu, I.K.M., Tsang, D.C.W., Cao, X., Lin, D., Wang, L., Graham, N.G.D., Alessi, D.S., Komárek, M., Ok, Y.S., Feng, Y., Li, X., 2019. Multifunctional iron-biochar composites for the removal of potentially toxic elements, inherent cations, and hetero-chloride from hydraulic fracturing wastewater. *Environ. Int.* 124, 521–532.
- Tanboonchuy, V., Grisdanurak, N., Liao, C. 2012. Background species effect on aqueous arsenic removal by nano zero-valent iron using fractional factorial design. *J. Hazard. Mater.* 205, 40–46.
- Tang, C., Zhang, Z., Sun, X., 2012. Effect of common ions on nitrate removal by zero-valent iron from alkaline soil. *J. Hazard. Mater.* 231 (6), 114–119.
- Tao, X., Hu, X., Wen, Z., Ming, Y., Li, J., Liu, Y., Chen, R., 2022. Highly efficient Cr(VI) removal from industrial electroplating wastewater over Bi₂S₃ nanostructures prepared by dual sulfur-precursors: Insights on the promotion effect of sulfate ions. *J. Hazard. Mater.* 424, 127423.
- Toli, A., Mystrioti, Christiana., Avgoustidis, I., Papassiopi, Nymphodora., 2021. Fixed-bed flow experiments with supported green nZVI for the remediation of contaminated waters: Effect of pH and background solution composition. *Chemosphere* 279, 130472.
- Vilardi, G., 2019. Mathematical modelling of simultaneous nitrate and dissolved oxygen reduction by Cu-nZVI using a bi-component shrinking core model. *Powder Technol.* 343, 613–618.
- Wang, C., Xu, Z., Ding, G., Wang, X., Zhao, M., Ho, S.S.H., Li, Y., 2015. Comprehensive study on the removal of chromate from aqueous solution by synthesized kaolin supported nanoscale zero-valent iron. *Desalin. Water Treat.* 57 (11), 5065–5078.
- Wang, X, Liu, F., Lu, L., Yang, S., Zhao, Y., Sun, L., Wang, S., 2013. Individual and competitive adsorption of Cr(VI) and phosphate onto synthetic Fe-Al hydroxides. *Colloids Surf. A: Physicochem. Eng. Asp.* 423, 42–49.
- Wang, Y., Chen, S., Yang, X., Wu, Y., Wang, S., 2019. Enhanced removal of Cr(VI) in the Fe(III)/natural polyphenols system: role of the in situ generated Fe(II). *J. Hazard. Mater.* 2019, 377, 321-329.
- Wei, Y., Liang, X., Wu, H., Cen, J., Ji, Y., 2021. Efficient phosphate removal by dendrite-like halloysite-zinc oxide nanocomposites prepared via noncovalent hybridization. *Appl. Clay Sci.* 213, 106232.
- Wen, Z., Zhang, Y., Da, C., 2014. Removal of phosphate from aqueous solution using nanoscale zerovalent iron (nZVI). *Colloid. Surface. A.* 457, 433–440.
- Wenzel, B.M., Marcilio, N.R., Godinho, M., Masotti, L., Martins, C.B., 2010. Iron and chromium sulfates from ferrochromium alloy for tanning. *Chem. Eng. J.* 165 (1), 17–25.
- Wu, Z., Su, Xiao., Lin, Zhang., Khan, N.I., Owens, G., Chen, Z., 2021. Removal of As(V) by iron-

- based nanoparticles synthesized via the complexation of biomolecules in green tea extracts and an iron salt. *Sci. Total Environ.* 764, 142883.
- Xiao, W., Ye, X., Zhu, Z., Zhang, Q., Zhao, S., Chen, D., Gao, N., Hu, J., 2020. Combined effects of rice straw-derived biochar and water management on transformation of chromium and its uptake by rice in contaminated soils. *Ecotoxicol. Environ. Saf.* 208, 111506.
- Xie, Y., Cwiertny, D.M., 2012. Influence of anionic cosolutes and pH on nanoscale zerovalent iron longevity: Time scales and mechanisms of reactivity loss toward 1,1,1,2-tetrachloroethane and Cr(VI). *Environ. Sci. Technol.* 46 (15), 8365–8373.
- Xu, B., Li, D., Qiang, T., Jiang, H., 2020. Boosting the activity and environmental stability of nanoscale zero-valent iron by montmorillonite supporting and sulfidation treatment. *Chem. Eng. J.* 387, 124063.
- Xu, J., Li, H., Lowry, L.G.V., 2021. Sulfidized nanoscale zero-valent iron: Tuning the properties of this complex material for efficient groundwater remediation, *Acc. Mater. Res.* 2 (6), 420–431.
- Xu, N., Huangfu, X., Li, Z., Wu, Z., Li, D., Zhang, M., 2019. Nanoaggregates of silica with kaolinite and montmorillonite: sedimentation and transport. *Sci. Total Environ.* 669, 893–902.
- Xu, Z., Wan, Z., Sun, Y., Gao, B., Hou, D., Cao, X., Komárek, M., Ok, Y.S., Tsang, D.C.W., 2022. Electroactive Fe-biochar for redox-related remediation of arsenic and chromium: Distinct redox nature with varying iron/carbon speciation. *J. Hazard. Mater.* 430, 128479.
- Yang, J., Wang, S., Xu, N., Ye, Z., Yang, H., Huangfu, X., 2021. Synthesis of montmorillonite-supported nano-zero-valent iron via green tea extract: Enhanced transport and application for hexavalent chromium removal from water and soil. *J. Hazard. Mater.* 419, 126461.
- Yao, Y., Mi, N., He, C., Zhang, Y., Ni, L., 2020. A novel colloid composited with polyacrylate and nano ferrous sulfide and its efficiency and mechanism of removal of Cr(VI) from water. *J. Hazard. Mater.* 399, 123082.
- Ye, Z., Xu, N., Li, D., Qiang, J., Du, C., Chen, M., 2021. Vitamin C mediates the activation of green tea extract to modify nanoscale zero-valent iron composites: enhanced transport in heterogeneous porous media and the removal of hexavalent chromium. *J. Hazard. Mater.* 411, 125042.
- Yi, Y., Wang, X., Ma, J., Ning, P., 2020. An efficient *Egeria najas*-derived biochar supported nZVI composite for Cr(VI) removal: Characterization and mechanism investigation based on visual MINTEQ model. *Environ. Res.* 189, 109912.
- Zeng, B., Pan, Z., Shen, L., Zhao, D., Teng, J., Hong, H., Lin, H., 2022. Effects of polysaccharides' molecular structure on membrane fouling and the related mechanisms. Social Science Electronic Publishing. *Sci. Total Environ.* 836, 155579.
- Zhang, C., Suen, C.L., Yang, C., Quek, Y., 2018. Antioxidant capacity and major polyphenol composition of teas as affected by geographical location, plantation elevation and leaf grade. *Food Chem.* 244, 109–119.
- Zhang, R., Xu, Y., Shen, L., Li, R., Lin, H., 2022. Preparation of nickel@polyvinyl alcohol (PVA) conductive membranes to couple a novel electrocoagulation-membrane separation system for efficient oil-water separation. *J. Membrane Sci.* 653, 120541.
- Zhang, Y., Jiao, X., Liu, N., Lv, J., Yang, Y., 2020. Enhanced removal of aqueous Cr(VI) by a green synthesized nanoscale zero-valent iron supported on oak wood biochar. *Chemosphere* 245,

125542.

- Zheng, H., Ren, X., Zhang, X., Song, G., Chen, C., 2019. Mutual effect of U(VI) and phosphate on the reactivity of nanoscale zero-valent iron (nZVI) for their co-removal. *J. Mol. Liq.* 297, 111853.
- Zhu, S.S., Huang, X.C., Wang, D.W., Wang, L., Ma, F., 2018. Enhanced hexavalent chromium removal performance and stabilization by magnetic iron nanoparticles assisted biochar in aqueous solution: mechanisms and application potential. *Chemosphere* 207, 50–59.

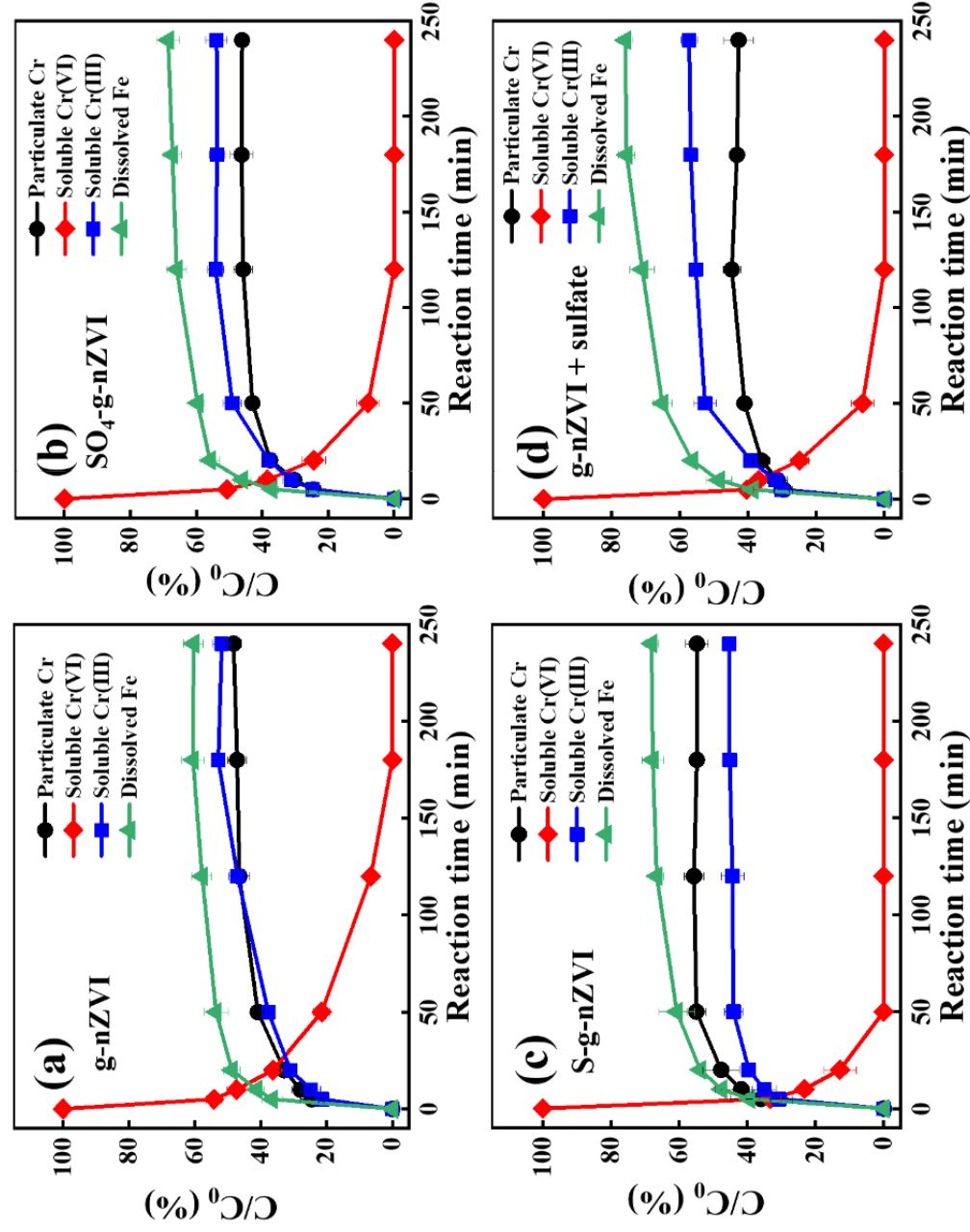


Fig. 1. Variations in Cr and dissolved Fe(III) of g-nZVI (a); SO₄-g-nZVI (b); S-g-nZVI (c); and g-nZVI in the presence of 1 mM sulfate (d) as a function of reaction time (initial Cr(VI) = 50 mg L⁻¹, material dosage = 0.5 g L⁻¹).

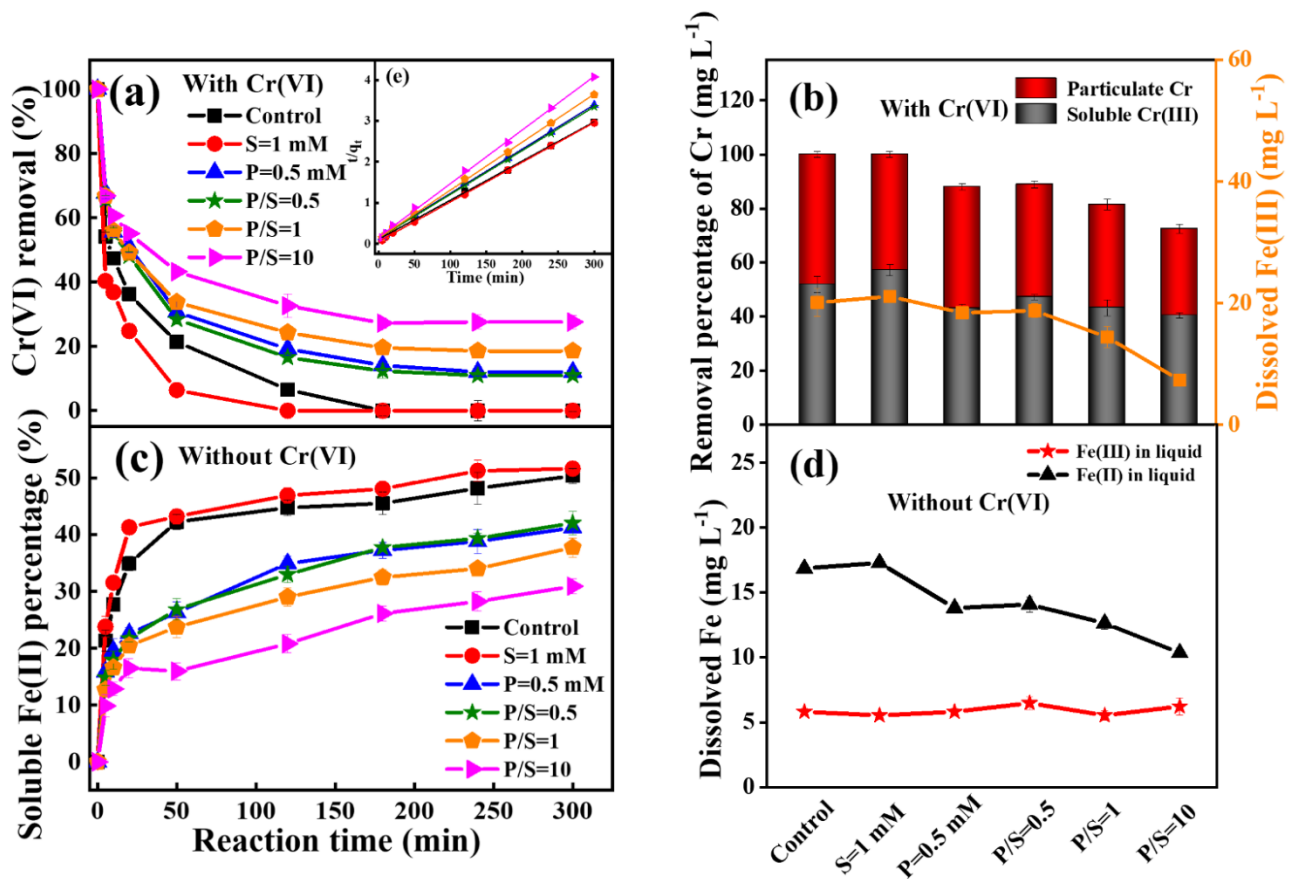


Fig. 2. Cr(VI) removal kinetics (a); Cr speciation (particulate Cr and soluble Cr(III)) variations (b); Fe(II) dissolution kinetics (c); and soluble Fe(II) and Fe(III) release amount from g-nZVI without Cr(VI) in the presence of (1 mM) sulfate (S); (0.5 mM) phosphate (P); and both with different molar ratios of P/S (0.5; 1 and 10) (d) (initial Cr(VI) = 50 mg L⁻¹, material dosage = 0.5 g L⁻¹).

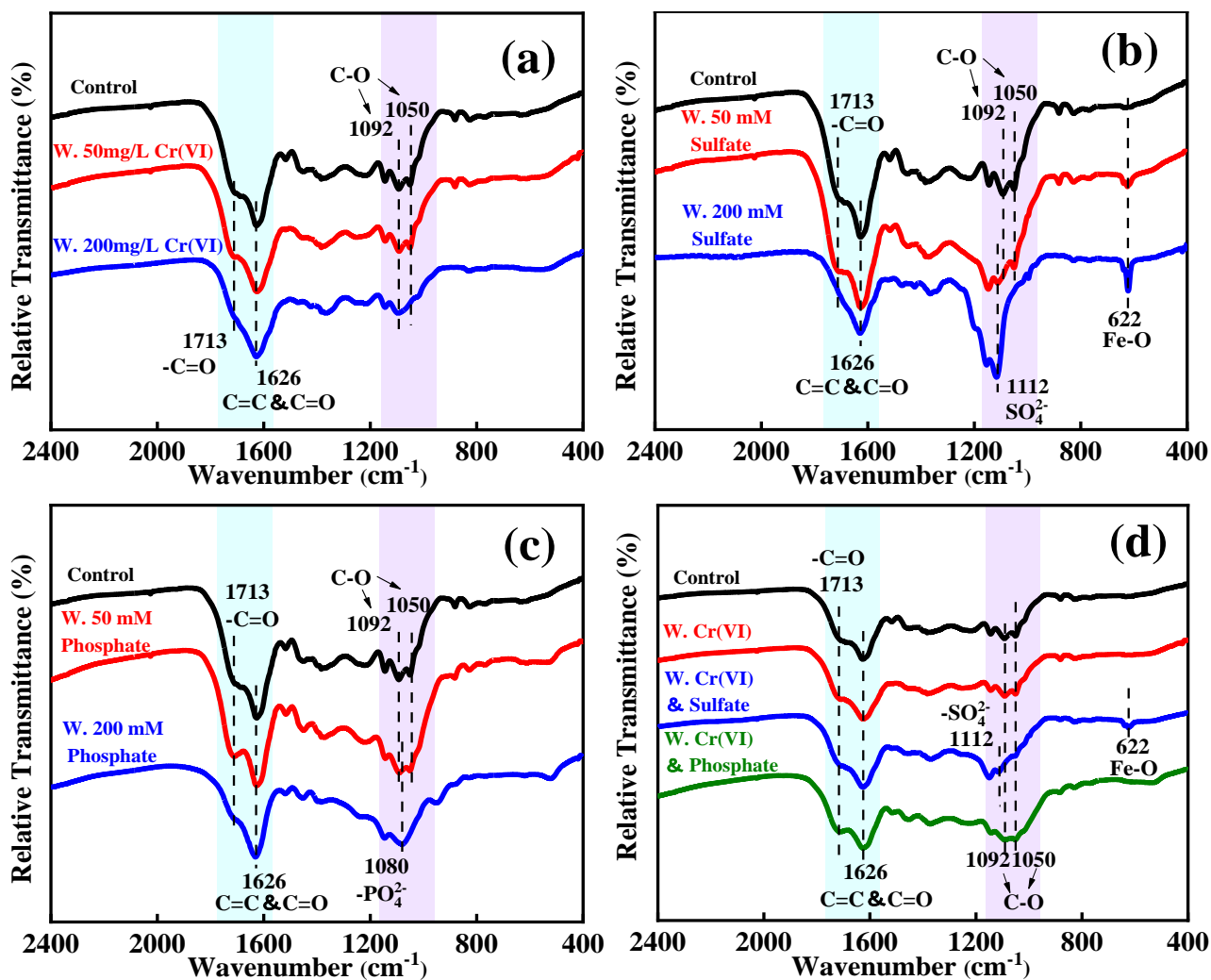


Fig. 3. FTIR spectra of 0.5 g L^{-1} g-nZVI reacting with Cr(VI) (a); sulfate (b); phosphate (c); and with Cr(VI) in the presence of sulfate or phosphate (d).

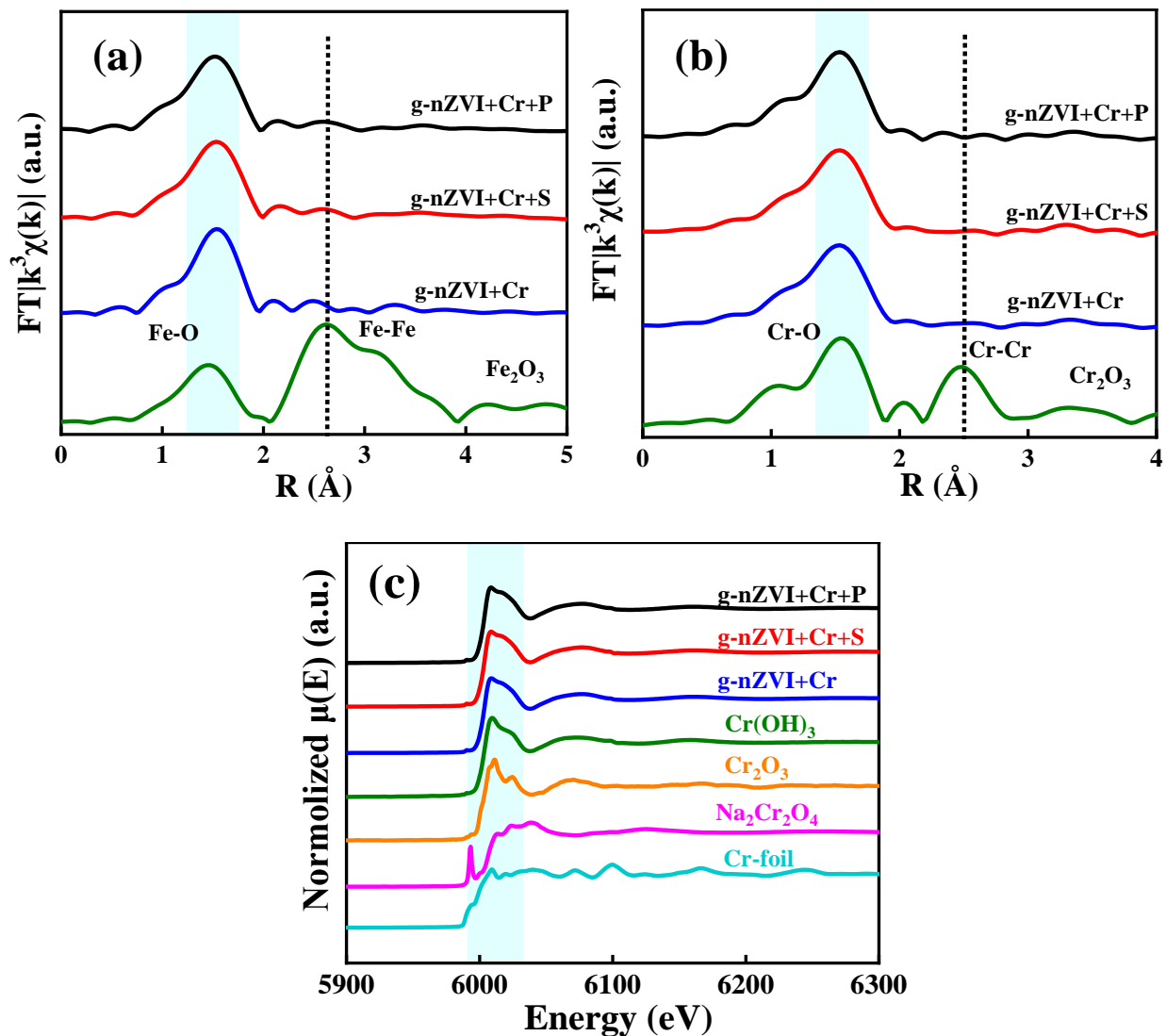


Fig. 4. Fourier-transformed Fe K-edge (a) and Cr K-edge (b) of XAFS spectra and Cr K-edge of XANES spectra (c) for 0.5 g L⁻¹ g-nZVI reacting with 50 mg L⁻¹ of Cr(VI) in the presence of sulfate (S) or phosphate (P).

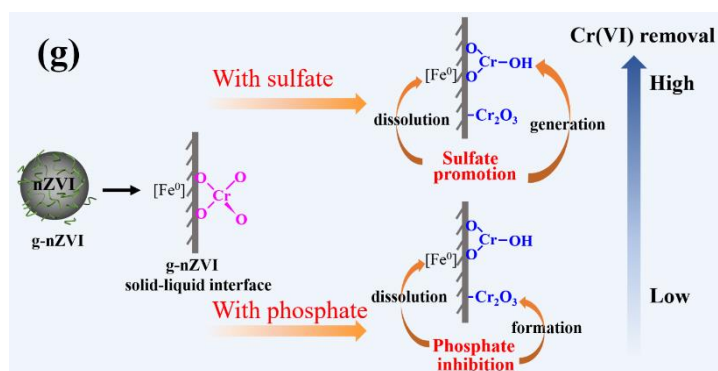
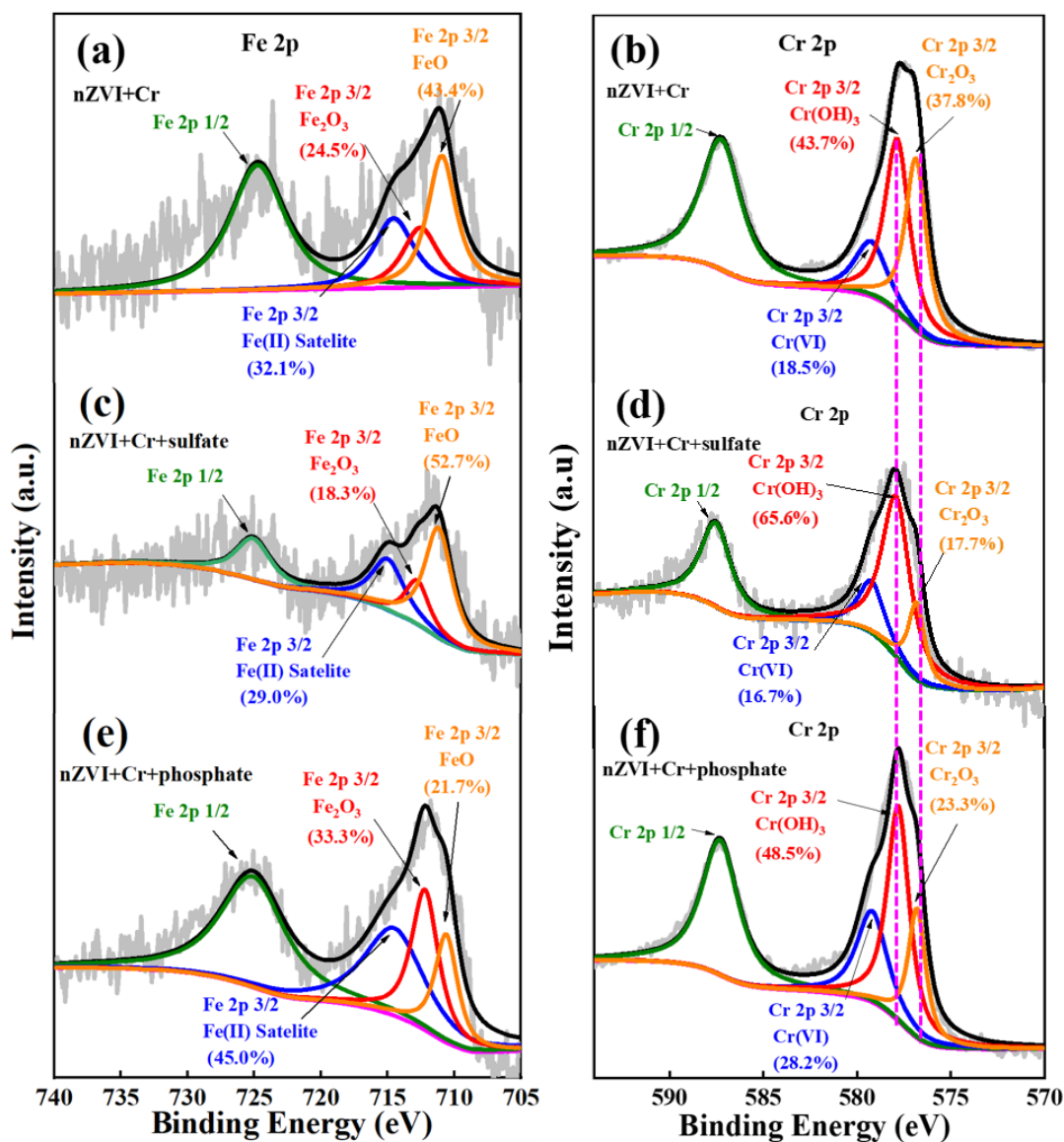


Fig. 5. XPS spectra of Fe 2p (a; c; e) and Cr 2p (b; d; f) for 0.5 g L⁻¹ g-nZVI reacting with 200 mg L⁻¹ of Cr(VI) (a; b) in the presence of sulfate (c; d) or phosphate (e; f); and the scheme of Cr(VI) adsorption and reduction processes in the solid-liquid interface of g-nZVI in the presence of sulfate and phosphate (g).